Electronic Supplementary Information

Highly Efficient NIR-II Photothermal Conversion from A 2,2'-Biquinoline-4,4'-Dicarboxylate based Photochromic Complex

Ning-Ning Zhang,[a] Ya-Tong Liu[a], Li Li[c], Xiang-Tong Liu[a], Ke Xu[a], Zhen-Yu Li[b] and Yong Yan*[,a,d]

[a]*School of Chemistry and Chemical Engineering, Liaocheng University, Liaocheng, Shandong 252000, P. R. China.*

[b]*School of Environmental and Materials Engineering, Yantai University, Yantai, 264005, P. R. China.*

[c]*School of Materials Science and Engineering, Henan Polytechnic University, Jiaozuo, 454000, P. R. China.*

[d]*State Key Laboratory of Structural Chemistry, Fujian Institute of Research on the Structure of Matter, Chinese Academy of Sciences, Fuzhou, Fujian 350002, P. R. China.*

**Email: yanyong1036@gmail.com (Y. Yan)*

Index

1. Table section

Table S1 Reported photothermal materials and their photothermal conversion efficiency (η) under the irradiation of a 1064 nm laser.

Items	η_{1064}	**Reference**
Complexes		
$[Sr(BCA)_2(H_2O)_2]_n$ (**1P**)	**84.5 %**	**This work**
Cu-THQNPs	51.34%	*ACS Appl. Mater. Interfaces,* 2018, **10**, 25203 – 25212
Au@MOF	48.5%	*Nano Lett.,* 2019, **19**, 6772 – 6780
rPMo·cTMB	48.4 %	*Adv. Healthcare Mater.,* 2022, **11**, 2102352
pMOF-a	32.2 %	*Chem. Commun.*, 2022, **58**, 11095 – 11098
THPTS-Pb	15.2 %	*Inorg. Chem.,* 2024, **63**, 3327 – 3334
COFs		
CNPs	50.6 %	*Chem. Commun.,* 2020, **56**, 7793−7796
Py-BPy-COF NPs	55.2 %	*J. Am. Chem. Soc.,* 2019, **141**, 14433 – 14442
HOFs		
TQC@PFC-1	32 %	*J. Mater. Chem. B,* 2023, **11**, 8649−8656
Organic Small molecules		
BAF4	80 %	*Angew. Chem. Int. Ed.,* 2021, **60**, 22376–22384
CY-1234	76.01 %	*Small,* 2023, 2307829
P-Pc-HSA	64.7 %	*RSC Adv.*, 2020, **10**, 22656 – 22662
2	62.26 %	*Angew. Chem. Int. Ed.,* 2024, e202400913
Zn_4-H_2Pc/DP	58.3 %	*Chem. Sci.*, 2019, **10**, 8246 – 8252
DAF-OH_2⊂GBox-4^{4+}	47.4 %	*Angew. Chem. Int. Ed.,* 2023, **135**, e202301267
DAF_2⊂GBox-4^{4+}	37.6%	
TTF_2⊂GBox-4^{4+}	39.9%	
CSM_2	31.6 %	*Mater. Horiz.,* 2020, **7**, 1379 – 1386

Polymers		
Y1	67.9 %	*Chem. Sci.,* 2021, **12**, 5177–5184
Y2	69.5 %	
Y3	76.5%	
PBBTDTS	65.0 %	*Chem. Commun.*, 2020, **56**, 1093 – 1096
SPNs3	60.0 %	*Chem. Commun.*, 2019, **55**, 9487 – 9490
HPW@PANI	57.76 %	*Int. J. Nanomed.*, 2022, **17**, 5565 – 5579
$2MPT^{2+}$•CB	54.6 %	*Angew. Chem., Int. Ed.*, 2019, **58**, 15526 – 15531
N1@2P	53.8 %	*Small,* 2023, **19**, 2300203
P_3	46.0 %	*ACS Nano*, 2019, **13**, 7345–7354
$NP^{PSP\text{-}P}t$	43.2 %	*Adv. Mater.,* 2023, *35*, 2300048
2NDTA	35 %	*Adv. Funct. Mater.,* 2024, 2401627
SPNs	21.2 %	*ACS Appl. Mater. Interfaces,* 2020, **12**, 33492–33499.
SP1	2.3 %	*Angew. Chem.Int. Ed.,* 2023, **62**, e202301617
SP2	46.4 %	
SP3	44.9 %	
SP4	46.5 %	
SP5	42.4 %	
Inorganic materials		
N-Doping CDs	81.3 %	*Carbon*, 2020, **162**, 220 – 233
AuPBs	80.8 %	*ACS Nano*, 2018, **12**, 2643 – 2651
Au_3Cu nanocrystals	75.2 %	*Nanoscale Horiz.*, 2018, **3**, 624 – 631
MoO_2 NPs	55.6 %	*Sci. China Mater.*, 2020, **63**, 1085 – 1098
CS–RuO_2 NPs	52.5 %	*Chem. Commun.*, 2020, **56**, 3019 – 3022
Pd Ncap	49.2 %	*ACS Appl. Mater. Interfaces*, 2023, *15*, 33, 39081–39098
Sb-Doped SnO_2	48.3 %	*Nanoscale*, 2018, **10**, 2542 – 2554
Ni_9S_8	46.0 %	*Nanoscale*, 2019, **11**, 20161 – 20170

Nb_2C (MXene)	45.6 %	*J. Am. Chem. Soc.*, 2017, **139**, 16235 – 16247
V_2C	45.0 %	*ACS Nano*, 2019, **13**, 1499 – 1510
$TeO_2/(NH_4)_xWO_3$ nanoribbons	43.6 %	*Nano Lett.*, 2019, **19**, 1179 – 1189
NIR-II-CD/BP hybrids	28.4 %	*ACS Appl. Mater. Interfaces*, 2019, **11**, 44949 – 44960
Si–Au	24.1 %	*J. Mater. Chem. B*, 2019, **7**, 4393 – 4401
EGaIn @SiO_2-RGD	22.43 %	*Nano Lett.*, 2019, **19**, 2128 – 2137
SnSe–PVP nanorods	20.3 %	*Mater. Horiz.*, 2018, **5**, 946 – 952
Au NSs	13.0 %	*J. Mater. Chem. B*, 2019, **7**, 2001 – 2008

Table S2. Crystal data and structural refinements for compound **1** and **1P**.

	1	**1P**
CCDC	2193840	–
Formula	$SrC_{20}H_{14}N_2O_6$	$SrC_{20}H_{14}N_2O_6$
Mr	465.95	465.95
Crystal size (mm^3)	0.42*0.05*0.03	0.45*0.05*0.03
Crystal system	monoclinic	monoclinic
Space group	I 2/a	I 2/a
***a* (Å)**	7.9349(6)	7.9351(4)
***b* (Å)**	11.4948(11)	11.4900(4)
***c* (Å)**	19.0537(19)	19.0417(8)
α (deg)	90	90
β (deg)	100.855(5)	100.829(2)
γ (deg)	90	90
***V* (Å^3)**	1706.8(3)	1705.20(13)
D_{calcd} (g/cm^3)	1.813	1.815
Z	4	4
F(000)	936.0	936.0
Abs coeff (mm^{-1})	3.204	3.207
R_1[a]	0.0253(1570)	0.0271(2106)

ωR_2[b]	0.0519(1743)	0.0595(2387)
GOF on F^2	1.066	1.065

[a] $R_1 = \sum||F_o|-|F_c||/\sum|F_o|$;
[b] $\omega R_2 = \{\sum\omega[(F_o)^2-(F_c)^2]^2/\sum\omega[(F_o)_2]^2\}^{1/2}$.

Table S3 List of the primary excited states for $[BCA^{2-}]^{\bullet\bullet}$ (the lowest singly unoccupied molecular orbital (SUMO) and the singly occupied molecular orbital (SOMO))

Excited State	Wavelength (nm)	Oscillator strength	Electronic transition (%)
7	**1164.33 nm**	0.0031	β-SOMO-3 → β-SUMO (75.9%)
9	**1065.88 nm**	0.0069	β-SOMO-8 → β-SUMO (72.8%)
10	**862.59 nm**	0.0340	α-SOMO →α-SUMO+1 (90.7%)
13	**650.95 nm**	0.0445	α-SOMO →α-SUMO+3 (68.7%)
14	**603.35 nm**	0.1006	α-SOMO →α-SUMO+2 (71.5%)
16	**556.14 nm**	0.0206	α-SOMO →α-SUMO+4 (79.5%)

Table S4 List of the molecular orbitals for **$[BCA^{2-}]^{\bullet\bullet}$**

Energy level	$[BCA^{2-}]^{\bullet\bullet}$	Energy level	$[BCA^{2-}]^{\bullet\bullet}$
α-SOMO (2.298 eV)	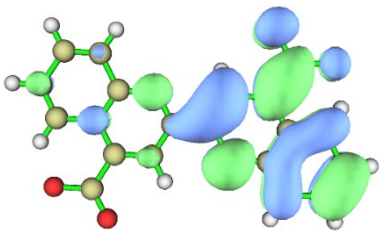	**β-SOMO-8** (-1.629 eV)	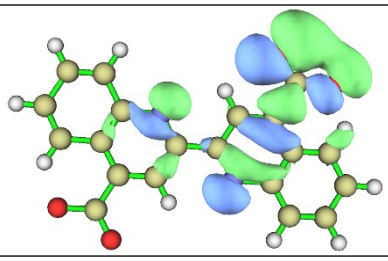

α-SUMO+1 (4.454 eV)	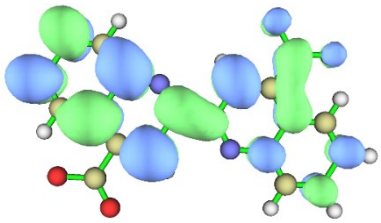	**β-SOMO-3** (-0.704 eV)	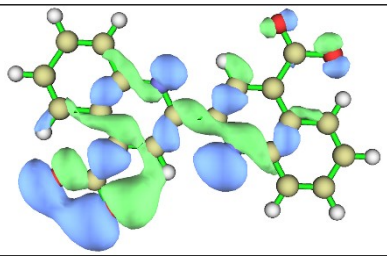
α-SUMO+2 (4.913 eV)	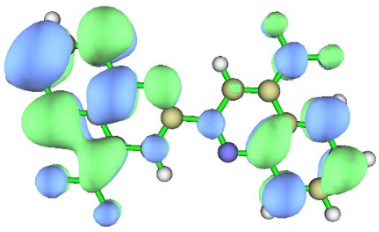	**β-SUMO** (0.783 eV)	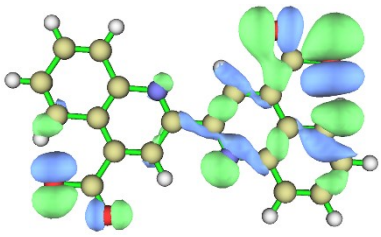
α-SUMO+3 (4.959 eV)	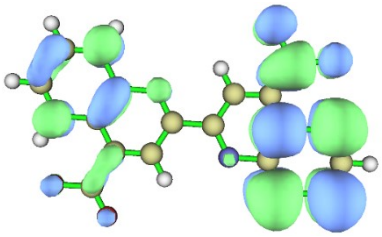		
α-SUMO+4 (5.229 eV)	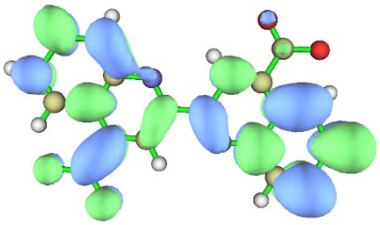		

Table S5 List of the primary excited states for **2[BCA^{2-}]$^{\bullet\bullet}$** (the lowest singly unoccupied molecular orbital (SUMO) and the singly occupied molecular orbital (SOMO))

Excited State	**Wavelength (nm)**	**Oscillator strength**	**Electronic transition (%)**
20	**1491.73 nm**	0.0021	β-SOMO-6→β-SUMO+1 (64.1%)
21	**1428.47 nm**	0.0097	β-SOMO-8→β-SUMO (70.0%)
23	**1371.72 nm**	0.0421	α-SOMO-1→α-SUMO (77.0%)
24	**1322.29 nm**	0.0019	β-SOMO-9→β-SUMO (66.3%)
25	**1288.29 nm**	0.0190	β-SOMO-11→β-SUMO (73.8%)
28	**1236.31 nm**	0.0128	β-SOMO-6→β-SUMO+1 (67.1%)
29	**1185.66 nm**	0.0059	β-SOMO-10→β-SUMO (93.2%)
45	**741.65 nm**	0.0039	α-SOMO→α-SUMO+4 (74.1%)
52	**644.74 nm**	0.1056	α-SOMO→α-SUMO+7 (62.6%)

Table S6 List of the molecular orbitals for **2[BCA^{2-}]$^{\bullet\bullet}$**

Energy level	2[BCA^{2-}]••	Energy level	2[BCA^{2-}]••
α-SOMO-1 (6.756 eV)	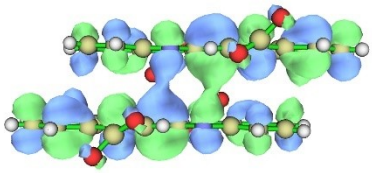	**β-SOMO-11** （3.266 eV）	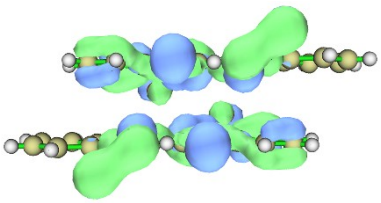
α-SOMO (7.065 eV)	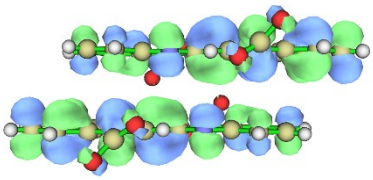	**β-SOMO-10** （3.347 eV）	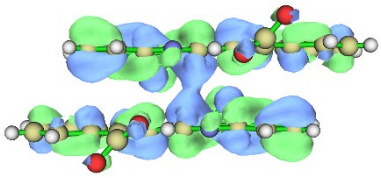
α-SUMO (8.164 eV)	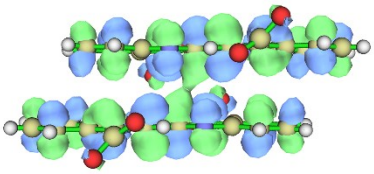	**β-SOMO-9** （3.370 eV）	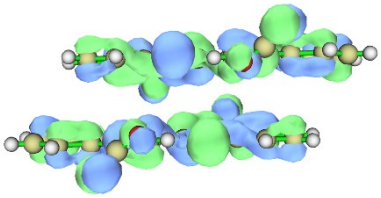
α-SUMO+4 （9.437 eV）	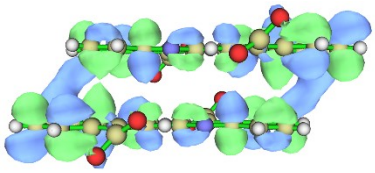	**β-SOMO-8** （3.381 eV）	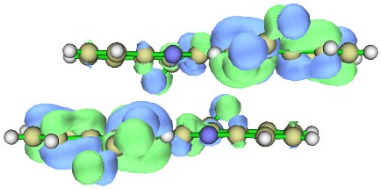
α-SUMO+7 （9.686 eV）	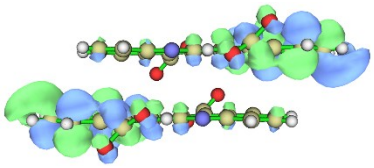	**β-SOMO-6** （3.642 eV）	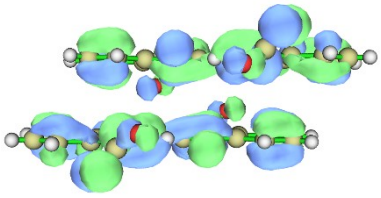
		β-SUMO （4.877 eV）	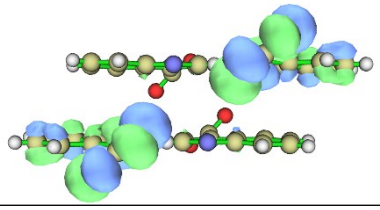
		β-SUMO+1 （5.081 eV）	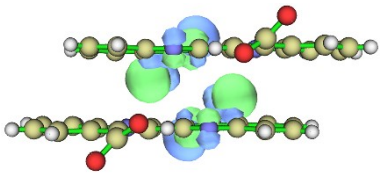

Table S7 Reported photochromic photothermal compounds and their photothermal conversion efficiency (η) under the irradiation of an 808 nm laser.

Items	η_{808}	**Reference**
NEU20	81.3 %	*Inorg. Chem. Front.,* **2023**, *10,* 3891–3898.
$\{[La_3(bcbp)_3(NO_3)_6O][La(NO_3)_6]_{1/3}\}_n$	77 %	*Chem. Commun.,* **2020**, *56,* 7399–7402.
$[Sr(BCA)_2(H_2O)_2]_n$ (**1P**)	**53.2 %**	**This work**
BPCA	41.9 %	*Angew. Chem. Int. Ed.,* **2023**, *62,* e202215591.
K-NDI	41.9 %	*Mater. Today Chem.,* **2023**, *27,* 101324.

2. Picture section

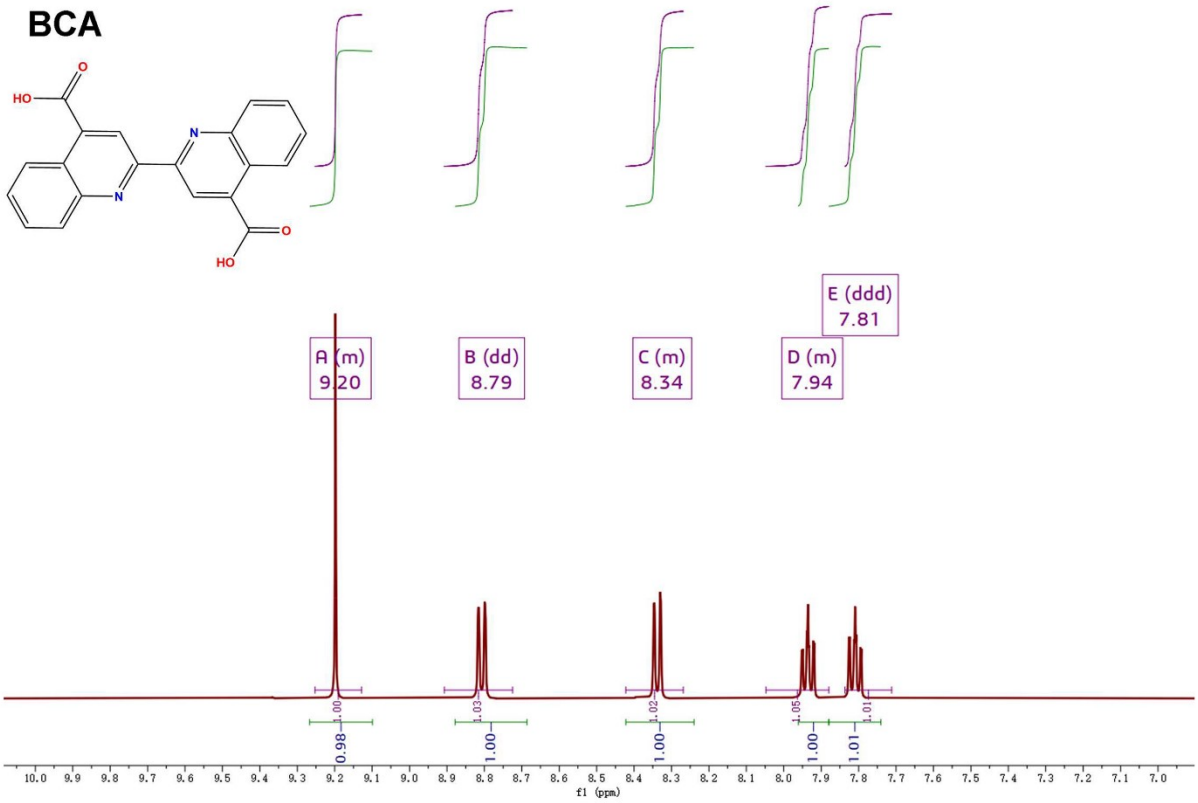

Fig. S1 ^{1}H-NMR spectrum of the BCA in DMSO-d_6.

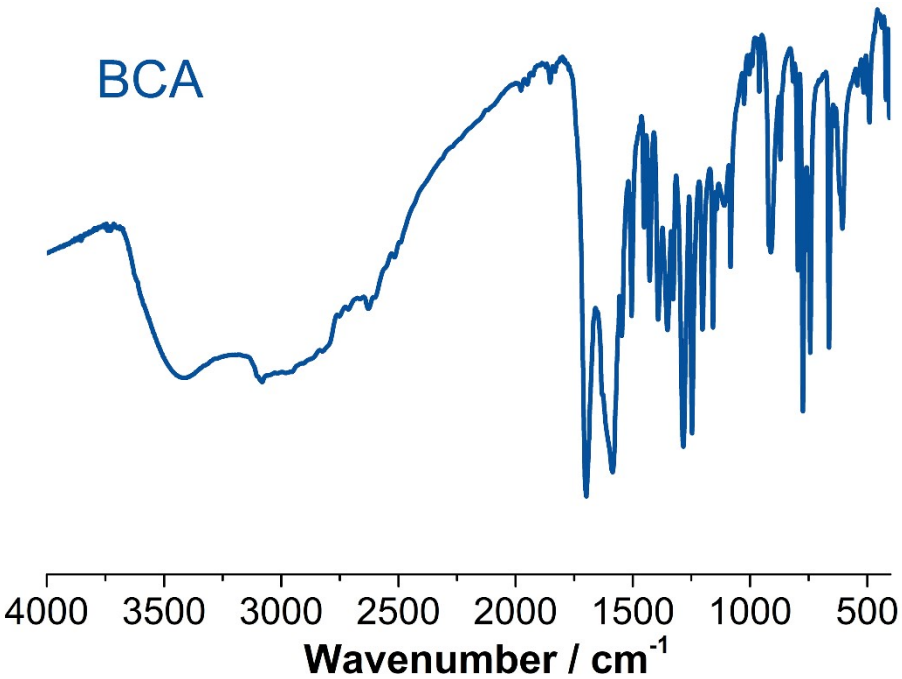

Fig. S2 IR spectrum of the BCA.

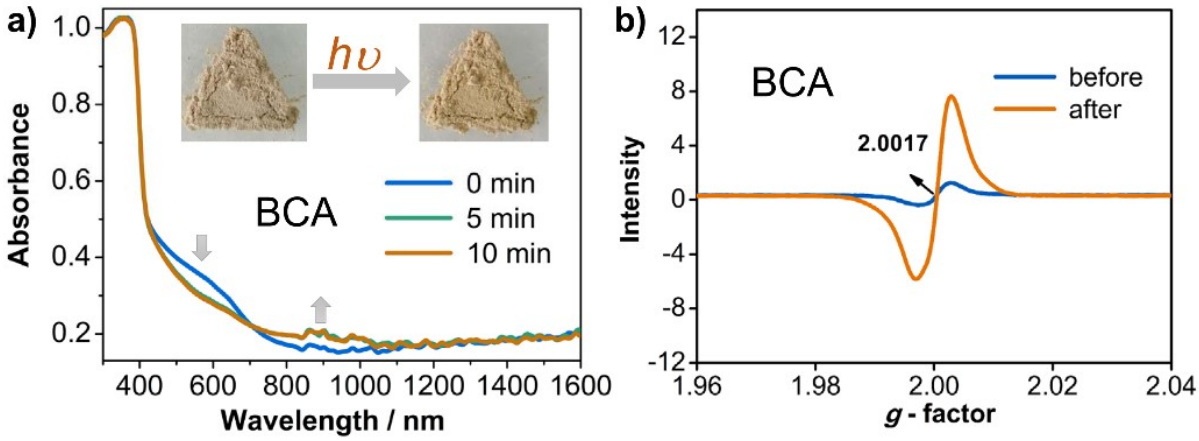

Fig. S3 (a) Time-dependent electronic absorption spectra (measured in the diffuse reflectance mode) of the BCA. Inset: photochromic behavior of the BCA under ambient environment. (b) EPR spectra of the BCA before and after irradiation in the solid state.

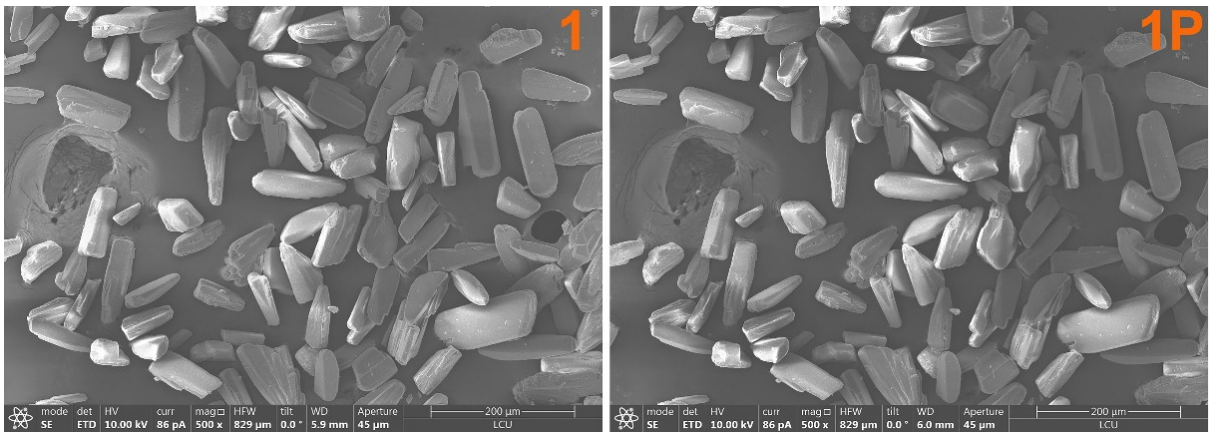

Fig. S4 SEM images of 1 (left) and 1P (right).

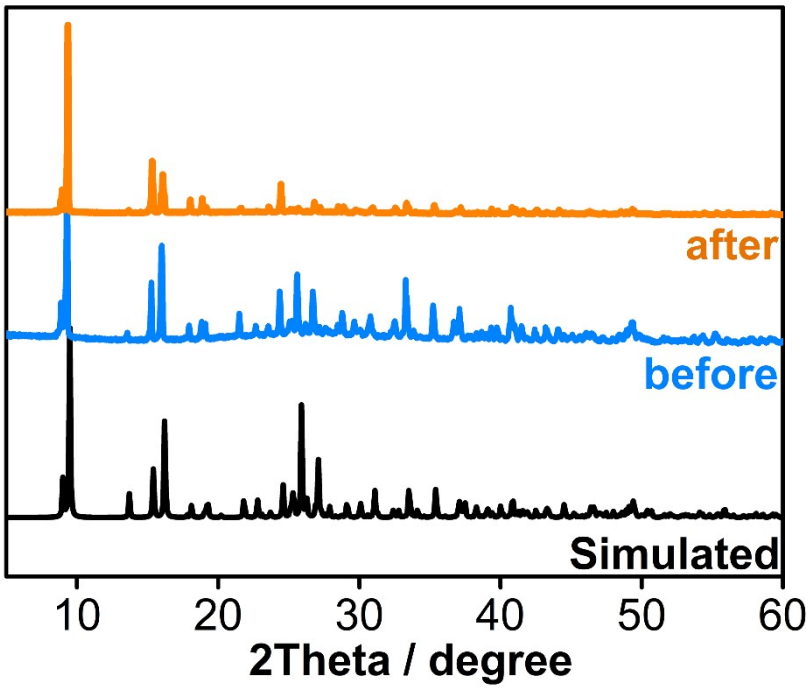

Fig. S5 PXRD patterns of compound **1**: **simulated**, simulated data using single-crystal data; **before**, measured data for as-synthesized samples; **after**, measured data for colored samples.

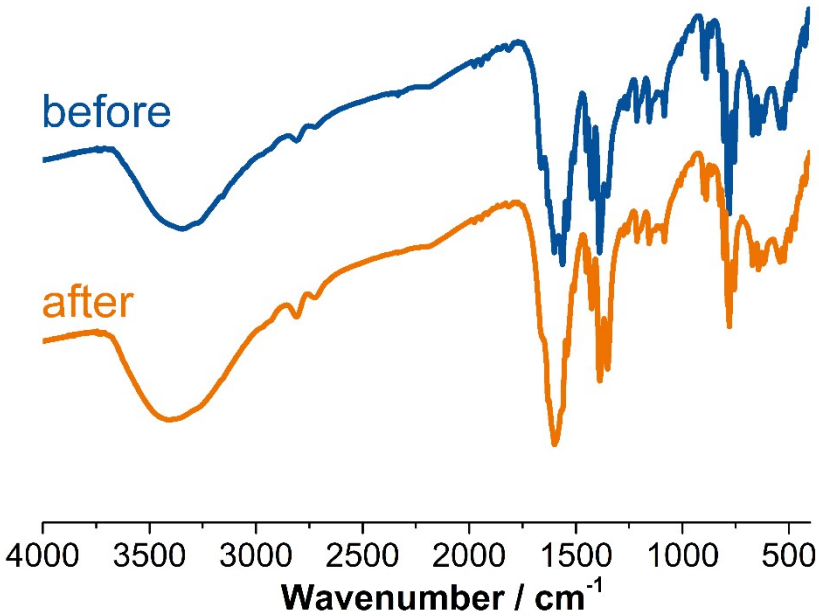

Fig. S6 IR spectra of compound **1**: **before**, measured data for as-synthesized samples; **after**, measured data for colored samples.

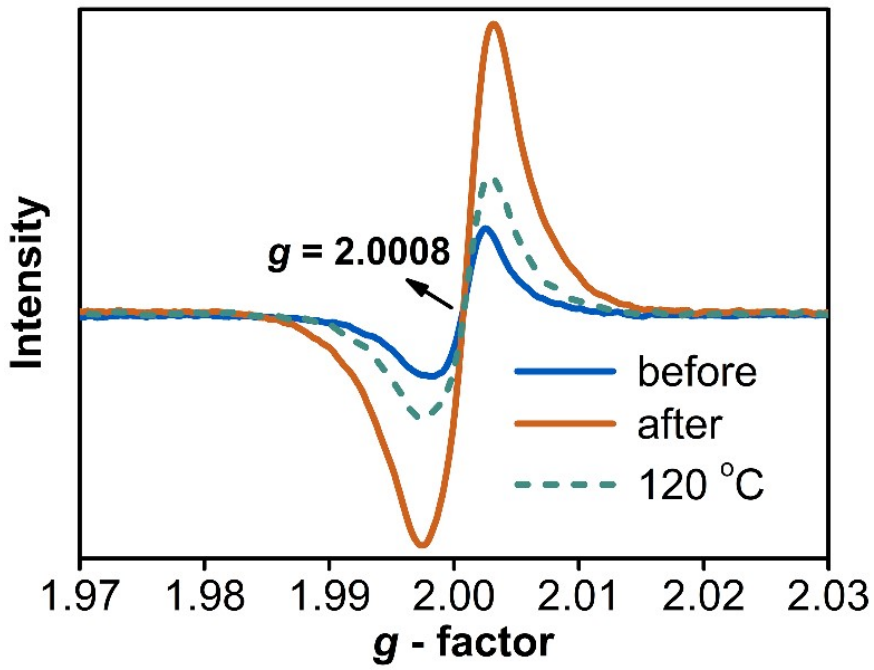

Fig. S7 Solid-state ESR spectra of complex **1** before and after irradiation by the Xe lamp for 3 min. The data for the irradiated samples after annealing at 120 °C for 2 hours is also shown.

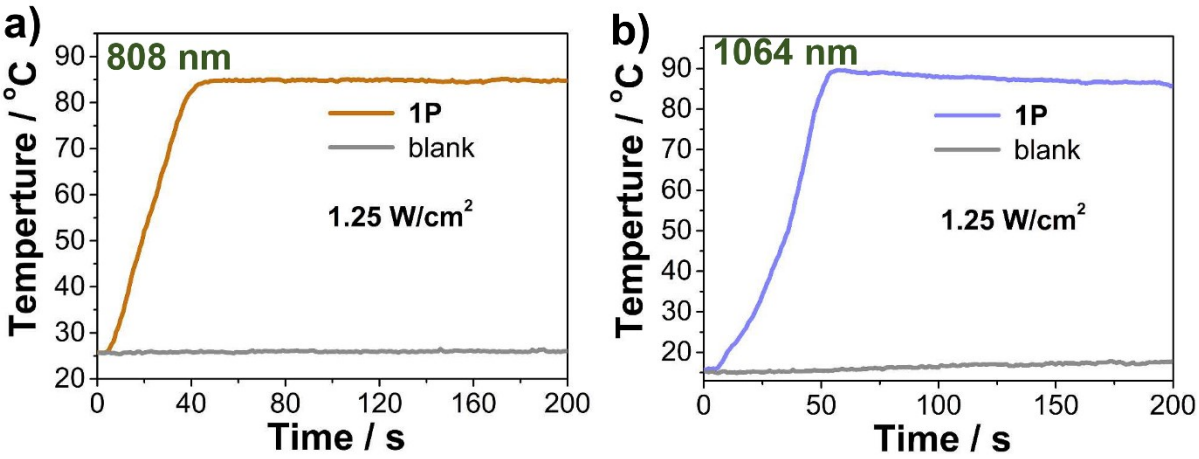

Fig. S8 Temperature curves of **1P** and blank quartz glass plate under the irradiation of the laser of 808 nm (a) and 1064 nm (b), respectively.

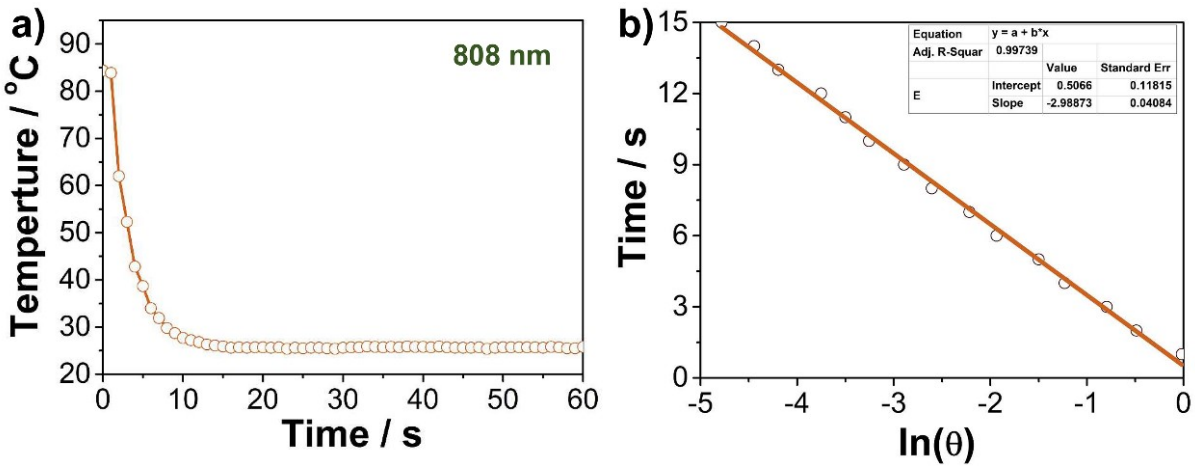

Fig. S9 Temperature decaying curve of **1P** after removing the laser source of 808 nm (1.25 W/cm^2) (a) and the corresponding time-lnθ linear curve (b). The photothermal conversion efficiency (η_{808} = 53.2 %) was calculated based on reported method[1]: $\eta_{808} = \frac{hS\Delta T_{max}}{I(1-10^{-A_{808}})}$, where the I is the laser power (1.25 W/cm^2), A_{808} is the absorbance of the samples at the wavelength of 808 nm (0.386, normalized F(R)), and ΔT_{max} is the maximum temperature change (61.5 K). hs can be calculated based on the formula of $\tau_s = \frac{\sum_i m_i C_{p,i}}{hs}$, where τ_s is the sample system time constant, m_i (0.017 g) and $C_{p,i}$ (1.12 J·(g·°C)$^{-1}$) are the mass and heat capacity of system components. When the laser switches off, τ_s can be estimated according to the formula: $t = -\tau_s \ln\theta$. The θ can be obtained according to the formula: $\theta = \frac{T - T_{surr}}{T_{max} - T_{surr}}$, where T is the temperature of sample, T_{max} is the maximum system temperature, and T_{surr} is the environment temperature.

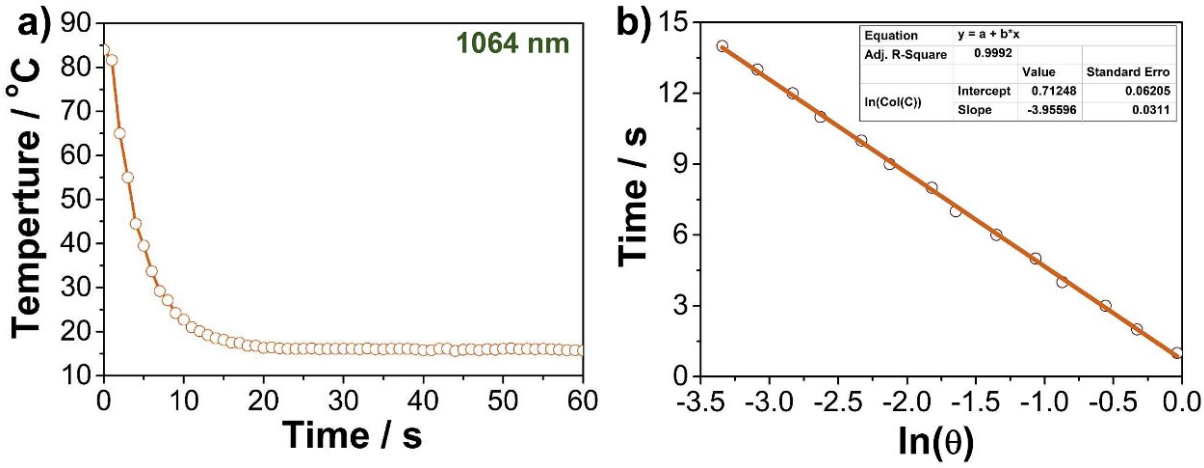

Fig. S10 Temperature decaying curve of compound **1P** after removing the laser source of 1064 nm (1.25 W/cm^2) (a) and the corresponding time-lnθ linear curve (b). The photothermal conversion efficiency (η_{1064} = 84.5 %) was also calculated based on reported method[1]: $\eta_{1064} = \frac{hS\Delta T_{max}}{I(1-10^{-A_{1064}})}$, where the I is the laser power (1.25 W/cm^2), A_{1064} is the absorbance of the samples at the wavelength of 1064 nm (0.290, normalized F(R)), and ΔT_{max} is the maximum temperature change (72.8 K). hs can be calculated based on the formula of $\tau_s = \frac{\sum_i m_i C_{p,i}}{hs}$, where τ_s is the sample system time constant, m_i (0.025 g) and $C_{p,i}$ (1.12 J·(g·°C)$^{-1}$) are the mass and heat capacity of system components. When the laser turns off, τ_s can be estimated according to the formula: $t = -\tau_s \ln\theta$. The θ can be obtained according to the formula: $\theta = \frac{T - T_{surr}}{T_{max} - T_{surr}}$, where T is the temperature of sample, T_{max} is the maximum system temperature, and T_{surr} is the environment temperature.

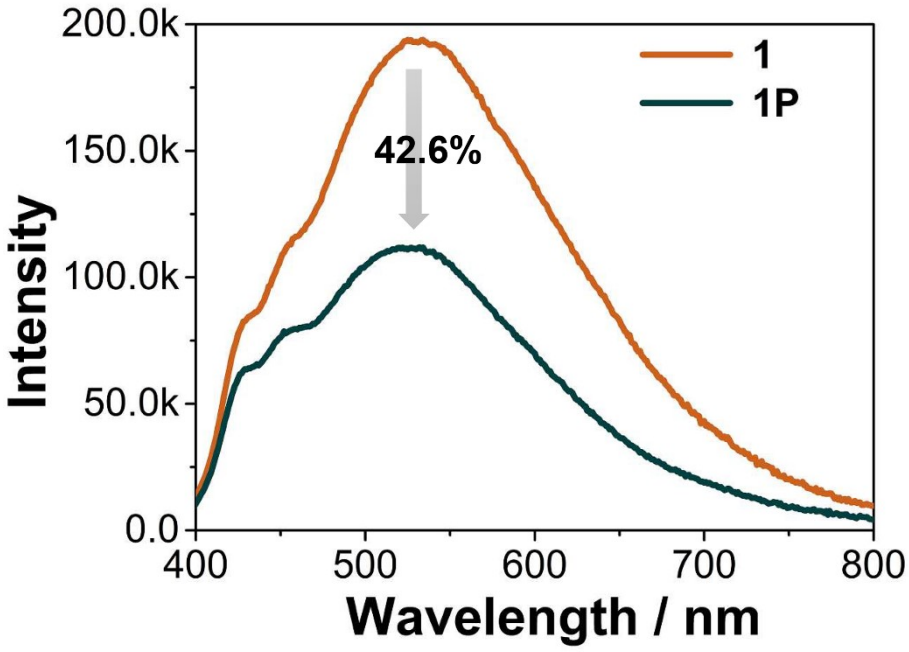

Fig. S11 Photoluminescence spectra of **1** and **1P** (λ_{ex} = 360 nm) at room temperature in air. It is obvious that the fluorescence of **1P** was decreased after photo irradiation, indicating the non-irradiative process in **1P** was enhanced by the photoinduced electron transfer process.

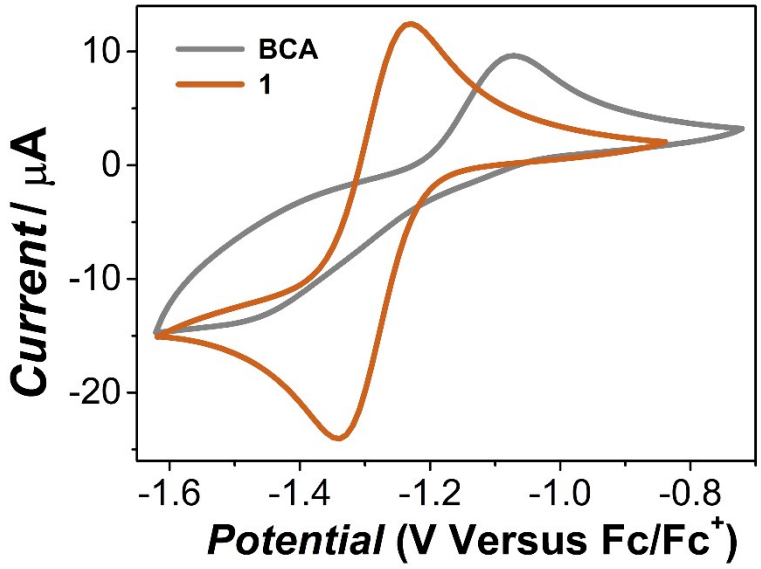

Fig. S12 Solid state cyclic voltammograms of **1** at 100 mV/s in a 0.1 M (n-Bu_4N)PF_6/CH_3CN electrolyte. And cyclic voltammograms of BCA at 100 mV/s in 0.1 M (n-Bu_4N)PF_6/DMF electrolyte. The solid-state cyclic voltammograms of **1** was measured using a three-electrode

cell at room temperature. About 4 mg of **1** powder were dispersed in a solution of 1 mL ethanol, 1 mL H_2O, and 20 μL of a 5% w/w Nafion solution in water and 1-propanol for 5 min. A 20 μl aliquot of the above dispersion was drop-cast onto the working electrode, a precleaned glassy carbon electrode, and dried in air. A Pt wire and an Ag/Ag^+ electrode acted as the counter and the reference electrode, respectively. Electrochemical measurements were carried out in 0.1M $[(n\text{-Bu})_4N]PF_6$ solution in acetonitrile under N_2 atmosphere. The reduction potentials of the **1** was obtained from the cyclic voltammogram and referenced with respect to Fc/Fc^+ as internal standard. The cyclic voltammogram of BCA was measured in 0.1 M $[(n\text{-Bu})_4N]PF_6$ solution in DMF under N_2 atmosphere. The concentration of BCA was about 5×10^{-3} mmol/mL. Ferrocene was used as internal standard.

References

1 S. Wang, S. Li, J. Xiong, Z. Lin, W. Wei and Y. Xu, *Chem. Commun.*, 2020, **56**, 7399–7402.